Air pressure measurement of circular thin plate using optical fiber multimode interferometer

Yufang Bai [a], Jie Zeng [a,*], Jiwei Huang [a], Zhenfeng Yan [a], Yaxing Wu [a], Kaiyu Li [b], Qiang Wu [c,d], Dakai Liang [a]

[a] *State Key Laboratory of Mechanics and Control of Mechanical Structures, Nanjing University of Aeronautics and Astronautics, 210016 Nanjing, China*

[b] *College Of Automation Engineering, Nanjing University of Aeronautics and Astronautics, 210016 Nanjing, China*

[c] *Faculty of Engineering and Environment, Northumbria University, Newcastle upon Tyne, NE1 8ST, U.K.*

[d] *Key Laboratory of Nondestructive Test (Ministry of Education) of Nanchang Hangkong University, 330063 Nanchang, China*

Abstract

In this paper, a simple singlemode-multimode-singlemode (SMS) optical fiber sensor is proposed and investigated for measuring the air pressure of a circular thin plate. Theoretical analysis and experimental demonstration are presents in this paper. The air pressure changes the strain and bending radius of the SMS sensor directly attached to the thin plate, and hence leads to shifts and intensity variation of the transmission spectrum. The relationship between transmission spectrum and pressure has studied by finite element method and optical simulation analysis. Experimental results show that the intensity-pressure and wavelength-pressure are −0.2718 dB/kPa and −106.7 pm/kPa in a pressure range of 70–130 kPa, respectively. The repeatability of the sensor is good, and the hysteresis rate is low. The key features of the proposed sensor are its simple structure and manufacturing process, low manufacturing cost. It can be used for high-precision pressure measurement.

Keywords: SMS optical fiber sensor; Multimode interference; Circular thin plate; Air pressure measurement.

1. Introduction

Optical fiber based pressure sensors have gained good acceptance due to their superior performance characteristics such as small size, immunity to electromagnetic interference and corrosion resistance. Various optical fiber sensors have been reported and employed for pressure measurement based on different mechanisms [1]. Optical fiber gratings are capable to measure pressure, such as normal FBG [2], chirped fiber grating [3] and long-period fiber grating (LPG) [4]. By adopting the wavelength difference between a pair of FBGs, Zhao *et al*.

* Corresponding author.

E-mail address: zj2007@nuaa.edu.cn (J. Zeng).

[2] developed a pressure sensor on the basis of diaphragm-cantilever with an accuracy of 258.28 pm/MPa. The tapered LPGs have been proven to monitor pressure in [4], where, this device exhibited a pressure sensitivity of 51 pm/MPa. However, the fabrication of grating sensors requires a complex process or expensive masks, and the length of the chirped grating and LPG is relatively long.

Optical pressure sensors based on concepts of special fibers are proposed, for instance, high-birefringence (Hi-Bi) fiber sensor [5] and photonic crystal fiber (PCF) sensor [6] are also good choices for pressure measurement. Chen *et al*. [5] reported a novel grating sensor inscribed on a Hi-Bi optical fiber, which can measure air pressure and temperature simultaneously. However, it requires a special fiber and complex drawing technique, which further increases the production cost. Since the PCF has the unique advantage of low dependence on temperature, PCF based pressure sensor has also been demonstrated in [6], but the cost of PCFs is expensive. Some structures fabricated based on multiple beam interference have been reported [7, 8]. The Fabry-Perot (FP) interferometric sensors have been also investigated in [9, 10], and the pressure sensitivities were obtained at −1.598 nm/kPa [9] and 1.336 nm/kPa [10], respectively. However, the configuration of FP sensor is relatively complex. Compared with the above sensors, multimode interference (MMI) based SMS sensors offer the advantages of low cost, simple structure, extreme flexibility and easy fabrication.

At present, the MMI occurs in the SMS structure has been investigated and developed to act as various sensors [11], such as temperature [12], refractive index (RI) [13], strain [14], curvature [15], etc. A sensitivity-enhanced strain gauge based on the model interference of a step-index fiber has been described, and its sensitivity is twice that of normal FBG [14]. Huang *et al*. [16] developed an SMS fiber structure based on the polymer multimode fiber (MMF), which the large detection range can reach 20000με and the sensitivity is −1.72 pm/με. However, due to the high thermal expansion coefficient and thermo-optic coefficient of the polymer fiber, it has a relatively high temperature-strain crosstalk of 33 με/°C. Gong *et al*. [15] proposed a curvature sensor by measuring the wavelength and intensity of the interference notch in its transmitted spectrum, and the maximum sensitivities are about −10.38 nm/m^{-1} and 130.37 dB/m^{-1} respectively. In addition, the novel curvature sensors using no-core fiber (NCF) [17, 18], three-core fiber [19], and seven-core fiber [20] instead of the traditional MMF section have been reported. Their curvature sensitivities can be further improved.

There are few researchers focusing on measuring air pressure using SMS structure. May-Arrioja *et al*. [21] investigated a pressure sensor based on polydimethilsiloxane (PDMS) polymer and NCF. The NCF directly contacted with PDMS layer which was previously attached to pressure sensitive membrane. The measurement sensitivity is -0.145×10^{-3} mW/kPa in the pressure range of 0–960 kPa. Although this sensor has been demonstrated to be feasible for measuring pressure, the sensitivity and resolution of pressure measurement are small. Besides, the thermal optics and thermal expansion effects of the polymer material lead to a strong dependence on temperature. The previous investigations have shown that the output spectrum of an SMS fiber structure depends on the length, the effective RI and the bending radius of the MMF section. The strain and bending applied to the MMF changes the length of the MMF and effective RI distribution along with MMF [22, 23], respectively. This induces the transmission loss and wavelength shift of the spectrum of the SMS fiber structure. By utilizing the characteristics that the SMS fiber structure is highly sensitive to bending, this paper provides a solution to pressure measurement.

In this paper, an SMS sensor is used to measure the air pressure of a small-size circular thin plate. This paper is organized as follows: in Section 2, the principle of strain and curvature measurement of sensors based on

multimode interference is illustrated; in Section 3, the design parameters of the sensor are determined by numerical analysis and finite element method (FEM); in Section 4, the construction of the test system is introduced, which is used to measure the transmission of sensors spectrum under different air pressure; and finally, conclusions of this paper are summarized in Section 5.

2. Sensing principle

A traditional SMS fiber structure is fabricated by splicing an MMF segment between two segments of singlemode fiber (SMF) [12], as shown in Fig. 1. The MMF section has a step-index profile. The high-order eigenmodes are excited in the MMF section when the input light field that propagating along the SMF coupled into the MMF. Then the interference between different modes occurs in the MMF, and recoupled into the output SMF [24]. Since the transmission spectrum of the SMS sensor depends on the effective RI and the length of MMF segment, when axial strain or bending is applied to MMF, the transmission spectrum of the SMS sensor will produce a shift. Suppose that the center axes of SMF and MMF align along the same axis perfectly, in the meanwhile, the SMF and MMF are circularly symmetric.

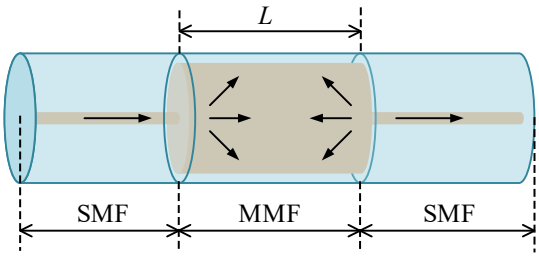

Fig. 1. A schematic diagram of SMS sensor.

The strain applied to the MMF changes its length, as well as the core radius and RI of the MMF. The interference between different modes occurs at the end of MMF. The minimum interference referred to the notch of the transmission spectrum in this paper. According to the condition of the wavelength at which the minimum interference occurs, the wavelength shift of the minimum interference intensity of the transmission spectrum caused by the strain at a constant temperature T can be obtained [14, 25]:

$$\frac{\Delta\lambda}{\lambda}=\left[\frac{\Delta n_{co}}{n_{co}}+\frac{2\Delta a}{a}-\frac{\Delta L}{L}\right]_T=-(p_e+2\upsilon_f+1)\varepsilon \tag{1}$$

where, the change of RI is calculated as:

$$\frac{\Delta n_{co}}{n_{co}}=-\frac{n_{co}^2}{2}\left[p_{12}-\upsilon_f(p_{11}+p_{12})\right]\varepsilon=-p_e\varepsilon \tag{2}$$

where, $\Delta L/L=\varepsilon$, $\Delta a/a=-\upsilon_f\varepsilon$, a is the radius of the MMF, υ_f is the Poisson's ratio of optical fiber, p_e is the effective photoelastic coefficient. It is clear that the strain sensitivity of the SMS sensor given by Eq. (1) is almost twice that of the normal FBG [14]. In addition, the direction of wavelength offset of SMS sensor is opposite to that of the FBG sensor, that is, the tensile stress applied to the SMS sensor will cause a blue shift of the wavelength.

Considering a deformed MMF with a nonzero curvature, the additional RI profile perturbation occurs in the fiber cross-section due to both geometric effects and stress-optic effects. The bend fiber in the coordinates of the Z plane is defined as an equivalent straight fiber in the coordinates of the W plane by using the conformal mapping method [26], this process is shown in Fig. 2. The RI of the equivalent straight fiber tilts with bending. Fig. 3 illustrates the RI distribution of the equivalent straight fiber, and for simplicity, the effective RI of the lowest order mode is drawn only.

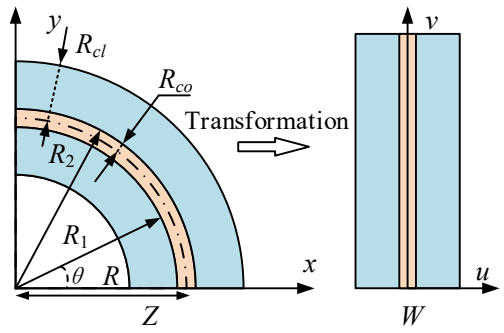

Fig. 2. Schematic diagram of the bent fiber with bending radius R and equivalent straight fiber achieved by conformal mapping.

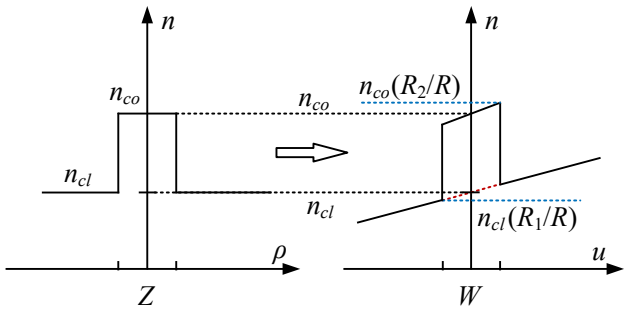

Fig. 3. Refractive index profiles of the bent fiber and equivalent straight fiber.

The modified refractive index n' of MMF (tilted profile) is calculated [27, 28]:

$$n' = n\left(1+\frac{u}{R_{eff}}\right) \tag{3}$$

where, R_{eff} is the equivalent bending radius which can be expressed as:

$$R_{eff} = \frac{R}{1-\frac{n^2}{2}\left[p_{12}-\upsilon_f(p_{11}+p_{12})\right]} \tag{4}$$

where, n is the refractive index of the straight fiber, R is the bending radius of the MMF. For the silica fiber, $R_{eff}/R = 1.28$. It can be seen from Eq. (3) that the refractive index of the fiber cross-section varies with the bending of the fiber, and it affects the interference between different modes in the MMF, resulting in the wavelength shift and intensity change of the output transmission spectrum of SMS sensor.

3. Thin plate model and sensor fabrication

3.1. Theory of bending and strain of thin plate

The schematic diagram of the thin plate configuration is shown in Fig. 4. In Fig. 4 (a), the red dotted box shows the cutaway picture of the structure. It consists of a thin plate, a pressure casing, fixed screw thread, pressure chamber, and SMS sensor, their geometrical dimensions are annotated in Fig. 4 (a). In order to give a universal internal screw thread application for the air inlet, the fixed M 20 × 1.5 screw thread was cut outside of the pressure chamber. The SMS sensor with a length of L is placed in the center of the thin plate along the radial direction by

epoxy resin adhesive, and it transfers the deformation of the plate to the SMS sensor. The sheaths are introduced to protect the optical fiber pigtail at both ends of the SMS sensor. The thin plate and the pressure casing are an integral structure. The thickness of the thin plate is 0.2 mm, and the thickness of the upper part of the pressure casing is 3 mm, which is much larger than that of the thin plate. Therefore, it is reasonable to assume a fixed boundary condition. That is, in theoretical analysis, the plate is clamped and under a uniform loading (air pressure), as shown in Fig. 5. The material property of the whole structure is a linear elastic material, and the material parameters used in the simulation and experiment in this paper is 361 L stainless steel, with the elastic modulus is 210 GPa and a Poisson's ratio is 0.27.

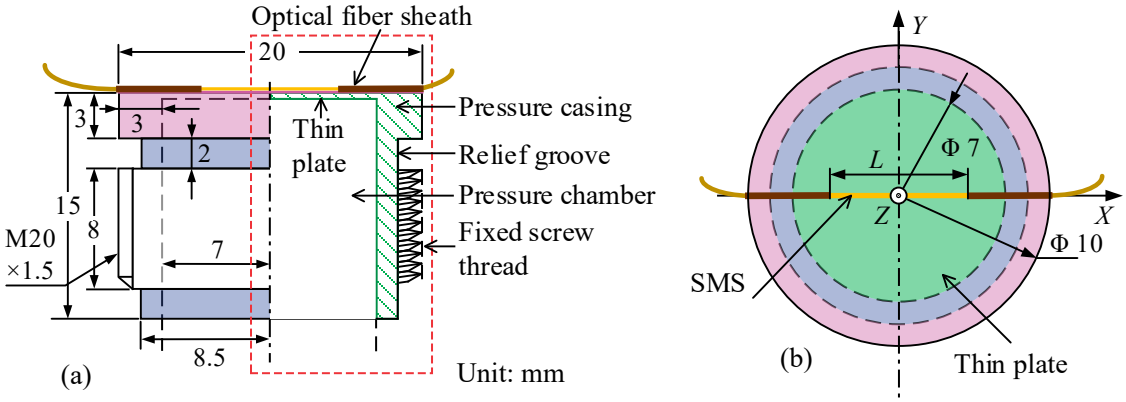

Fig. 4. Schematic diagram of the thin plate configuration. (a) Side view schematic; (b) Top view schematic.

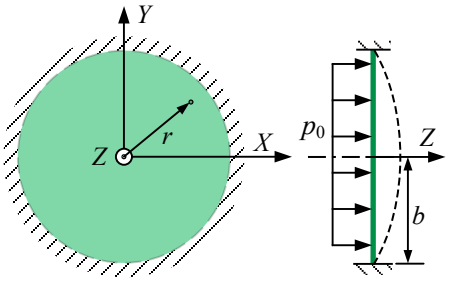

Fig. 5. Simplified diagram of thin plate with clamped edges under a uniform load.

When the distributed air pressure load p_0 is injected into the pressure chamber, the circular thin plate will be deformed due to the pressure difference on the two sides of the plate. The plate is clamped edge under a uniform load (as shown in Fig. 5), then the boundary condition are:

$$w(r)\big|_{r=b} = 0\,,\ \left.\frac{dw(r)}{dr}\right|_{r=b} = 0 \tag{5}$$

where, $w(r)$ is the deflection in the z direction of the thin plate, r is the radial radius from the center point to arbitrary point of the plate, $0 \le r \le b$. According to the general assumption of the thin plate bending theory, the strain perpendicular to the neutral plane can be ignored, and the third principal stress σ_z is much smaller than that of the stress components in the other directions, so the deformation caused by it can be ignored. Therefore, the corresponding principal stress under the polar coordinate system can be expressed as [29]:

$$\sigma_r = \frac{12M_r}{h^3}z,\ \sigma_t = \frac{12M_t}{h^3}z,\ \tau_{rt} = \tau_{tr} = \frac{12M_{rt}}{h^3}z \tag{6}$$

$$M_r = \frac{p_0}{16}\left[(1+\upsilon_p)b^2 - (3+\upsilon_p)r^2\right] \tag{7}$$

$$M_t = \frac{p_0}{16}\left[(1+\upsilon_p)b^2 - (1+3\upsilon_p)r^2\right] \tag{8}$$

where, σ_r , σ_t and τ_{rt} are radial normal stress, tangential normal stress and shear stress, respectively; M_r , M_t and M_{rt} are radial bending moment, tangential bending moment and torque respectively; b , h and υ_p are the radius, thickness and Poisson's ratio of the thin plate respectively; p_0 is the distributed air pressure applied on the circular thin plate. Using the conversion formula from the polar coordinate system to the Cartesian coordinate system, combined with Hooke's law, the strain along the radial direction on the neutral surface $z = h/2$ of the thin plate can be derived, and its calculation formula is as follows [30]:

$$\varepsilon = \frac{1}{E_p}\left(\sigma_X - \upsilon_p\sigma_Y\right) = \frac{1}{E_p}\left(\sigma_r - \upsilon_p\sigma_t\right) \tag{9}$$

where, E_p is the elastic modulus of the plate, σ_X and σ_Y are the normal stress in X and Y directions, respectively. It can be seen from Eqs. (6)–(9) that the strain on the surface of the thin plate increases with the increase of external pressure, and the strain along the X-direction of the plate has a linear relationship with the distributed pressure.

The deflection $w(r)$ of the circular thin plate under uniform external pressure is calculated by:

$$w(r) = \frac{p_0(b^2 - r^2)^2}{64D}, \quad 0 \le r \le b \tag{10}$$

where, $D = E_p h^3 / \left(12(1-\upsilon_p^2)\right)$ is the bending stiffness of the thin plate. Then, the maximum deflection occurs at the center of the circular thin plate, it can be calculated as follows:

$$w_{\max} = \frac{p_0 b^4}{64D} \tag{11}$$

According to the curvature definition of the plane curve, the curvature can be obtained:

$$K = \frac{w''(r)}{(1+w'(r)^2)^{3/2}} \tag{12}$$

When the circular thin plate is subjected to air pressure, both strain and curvature will be applied to the SMS sensor simultaneously. By using Eq. (10), the displacements along the central axis of the plate are calculated under uniform pressure loads of 50 kPa, 100 kPa and 200 kPa, as shown in Fig. 6 (a), and as the pressure increases the deflection of the plate increases. The deflection of the thin plate decreases along the radial direction starting at the

center point, with the maximum deflections being 0.01242, 0.02484 and 0.04969 mm, respectively, occurring at the center of the plate. According to Eq. (12), the curvature response of the central axis of the thin plate to different pressure is calculated, as shown in Fig. 6 (b). It can be obtained that curvature is not a constant but varies along the radial direction of the thin plate. The curvatures of the thin plate center point at different air pressures are 1.018, 2.035 and 4.071 (unit: 10^{-3} mm^{-1}), respectively. In addition, Patran software was also applied to verify the distribution of the strain and displacement. Since the structural model is symmetric, half of the model is used for simulation. Fig. 6. (c) gives the displacement distribution cloud diagram of the sensing part (top part) of structure, and the air pressure applied to the thin plate is 50 kPa.

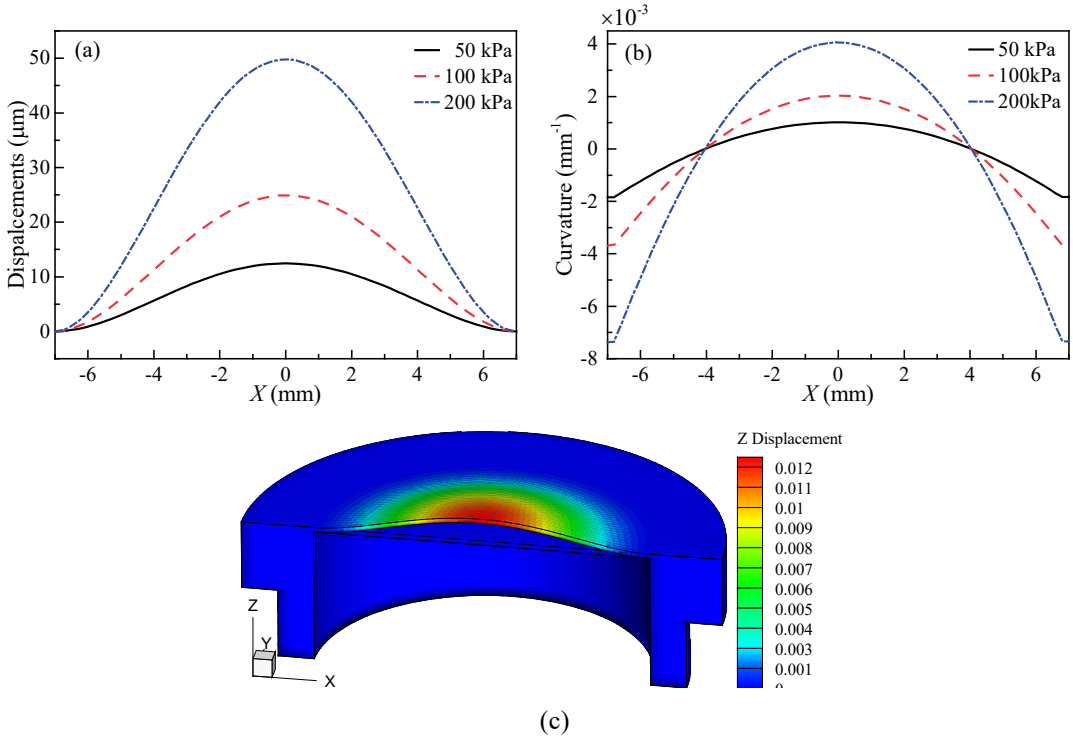

Fig. 6. Simulated (a) displacements and (b) curvature along the central axis of thin plate; (c) displacements distribution when the applied pressure is 50 kPa.

3.2. Sensor fabrication

The key component of the SMS sensor is the MMF, and multimode interference in planar waveguides has been intensively studied. In order to describe the light propagation within the MMF section, a numerical simulation was carried out by using the beam propagation method (BPM). In the simulation example, the diameters of core/claddings for standard SMF (SMF-28) and MMF are 8.2/125 μm and 105/125 μm, respectively. The refractive index core/claddings of SMF and MMF are 1.4504/1.4447 and 1.4446/1.4271, respectively. The input free-space wavelength is 1550 nm. Fig. 7 displays the amplitude distribution inside the MMF section with a length of 45 mm. It is found that when light is emitted from the SMF to the MMF interface, the light has different amplitude distributions at different distances due to the MMI effect of the MMF. The periodic light transmission patterns will also be produced within MMF [24]. It can be seen that the self-imaging occurs at the position of about 43 mm, which has the highest intensity. When the propagation distance is 10733 μm, an image formed by converged light is known as quasi-image [31]. Note that the diameter of the thin plate is 14 mm, and in order to avoid the influence of concentrated stress on the fixed edge of the thin plate, the length of 1 mm should be reserved

away from the fixed edge, that is, the effective length can be used for sensor adhesion is 12 mm. In addition, since the length of 10733 μm is a quasi-image distance, some notches formed by multimode interference appear around this length. In this paper, these notches are used for pressure measurement, so this length is used for simulation analysis of the sensor is reasonable. The sensor is designed and fabricated around this length.

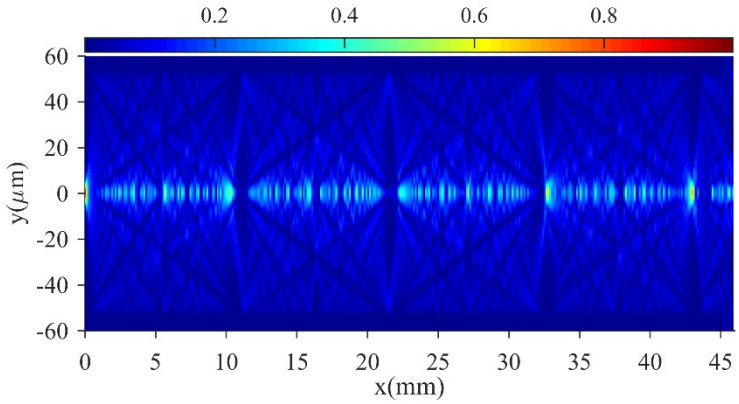

Fig. 7. Simulated amplitude distribution of optical fields of MMF at a wavelength of 1550 nm using BPM.

To obtain the optimized length of MMF, transmission losses for the desirable wavelength, from 1510 nm to 1580 nm, are scanned around the length from 8.5 mm to 11.0 mm. Fig. 8 (a) illustrates the simulated transmission loss of the SMS sensor as a function of the length of MMF and the free-space wavelength. The maximum and minimum peaks of the output transmission spectrum corresponding to different free-space wavelengths appear in different multimode fiber lengths. The transmission spectra of MMF with a length range of 8.5–11 mm at the wavelength of 1520 nm and 1564 nm, respectively, shown in Fig. 8 (b). It can be observed that when the length of the MMF is equal to the propagation length for the quasi-image, the intensity reaches a maximum value. The transmission distance of the notch caused by mode interference is less than the quasi-imaging length of the output transmission spectrum.

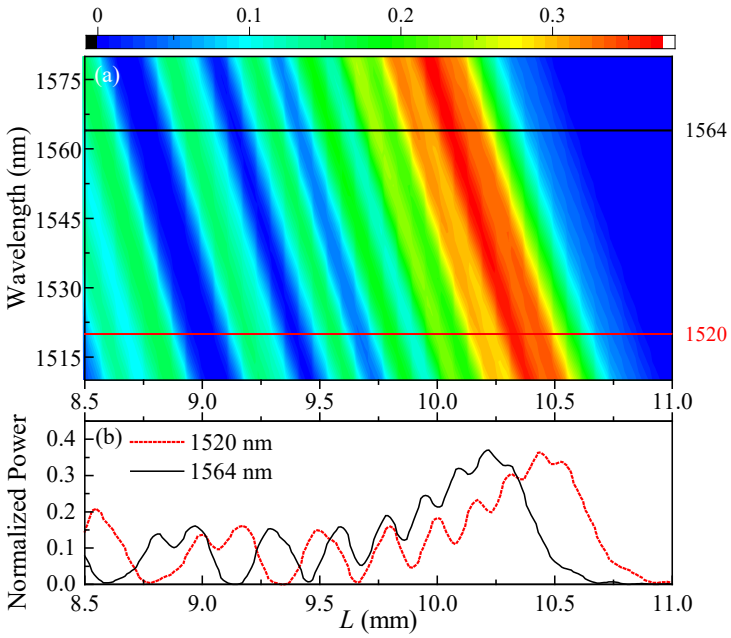

Fig. 8. Simulated transmission spectrum of the SMS (a) at a wavelength range of 1510–1580 nm and the length of MMF is 8.5–11 mm, (b) at the wavelength of 1520 nm and 1564 nm.

The notches of the transmission spectrum are used for the pressure measurement in this paper. Therefore, it is necessary to obtain several lengths with effective notches of transmission spectrum within the measured wavelength range. The optimized lengths of MMF related to the notches of the spectrum are around 9.53 mm, 9.31 mm and 8.95 mm, respectively, and the variation of transmission spectrum at different lengths is analyzed, as shown in Fig. 9. The conclusion that the change of MMF length causes the shift of the transmission spectrum can be obtained. It is mainly manifested as the blue shift of the wavelength at the notches (Dip) of the corresponding transmission spectrum when the length of MMF becomes longer, and conversely, the red shift occurs. Ignoring the radial contraction of multimode fiber, the main response of sensor to strain is the offset of the wavelength, and the effect of strain on the intensity of transmission spectrum can be negligible.

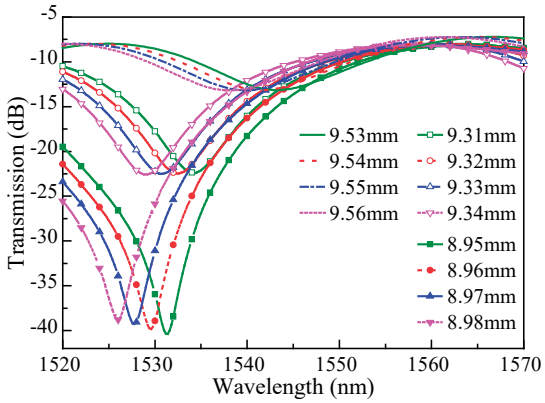

Fig. 9. Simulated transmission spectral responses of different length of MMF.

The light amplitude profile of MMF with length of 10733 μm and a bending radius of 29.8 mm is shown in Fig. 10 (a). As the curvature is applied on MMF, the modified refractive index illustrated by Eq. (3) is asymmetrical, therefore, the amplitude profile of the light field in MMF is also asymmetrical. The relationships between the transmission losses and curvature for the above different lengths of MMF are plotted in Fig. 10 (b). A better choice of the length for the MMF section is determined by the calculation result, and the output can be strongly dependent on wavelength and intensity. The response spectra with different lengths of MMF of SMS sensor are simulated, and the relationship between the loss of transmission and curvature is shown in Fig. 11 (b). The transmission loss curve of the sensor with the length of MMF 9.53 mm is almost linear over the curvature range compared with other curves. Then, the response spectra are simulated when the length of the MMF is 9.53 mm, as shown in Fig. 11 (a). It can be seen that the wavelength of the output transmission spectrum at Dip shifts blue with the increase of the curvature (1/bending radius) of the multimode fiber, and the loss of transmission intensity gradually increases with the increase of the curvature.

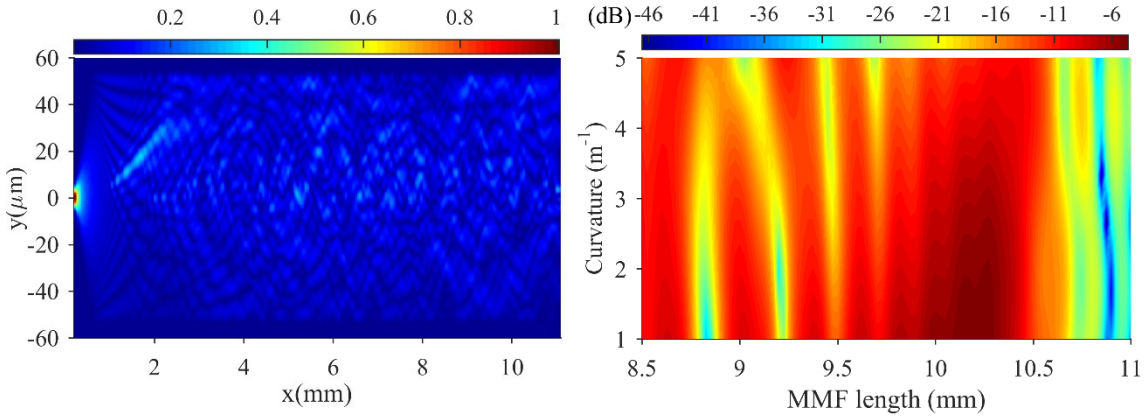

Fig. 10. Simulated amplitude distribution of bend MMF.(a) Simulated amplitude distribution of bend MMF at a wavelength of 1550 nm; (b) Transmission loss versus the curvature and length of MMF;

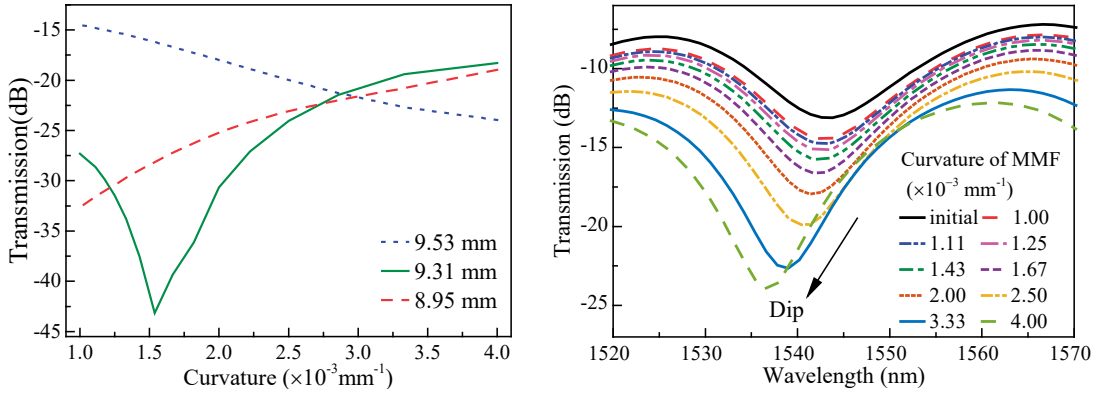

(a) Relationship between the transmission loss and curvature; (b) The transmission spectrum under different curvature.

Fig. 11. Simulated transmission spectral responses of different curvature of MMF.

The sensitivity of the sensor is related to the behaviour of the wavelength, length, width (radius) and refractive index change of the multimode fiber. The relationship between other operation parameters and length variation is [32]:

$$\frac{\delta L}{L} = 2\frac{|\delta a|}{a} \square \frac{|\delta \lambda_0|}{\lambda_0} \square \frac{\delta n_r}{n_r} \tag{13}$$

It is obvious that when the radius of the multimode fiber is larger, the wavelength of the transmission spectrum is more dependent on the change of the length of the MMF. Using the above analysis results, a step MMF with a diameter of 105 μm and a length of 9.53 mm is used to fabricate the sensor for measuring air pressure. The SMF (SMF 28) and MMF (SI 105/125-22/250, YOFC) used in the experiment were fused together by a fusion splicer (Fujikura 80S, Japan).

It also needs to be noted that the MMF segment of the SMS sensor structure is relatively short, it should be cut precisely to ensure the accuracy and reproducibility of the sensor. There are some precision cutting devices are used to prepare the SMS structure. High precision cleaver and high grade fiber polishing papers can precisely control the length of MMF [33]. A precise cutting system was employed to be used for the fabrication of the

sensor. This system comprises a coaxial 3D precision displacement platform to determine the cutting position, a fiber cleaver, and a microscope to determine the splicing point [34, 35].

4. Experimental results and analysis

4.1. Air pressure experimental setup

The entire air pressure measurement system is presented in Fig. 12, all measurements were carried out under the condition of a stabilized room temperature. In the experiment, the SMS sensor was uniformly adhered to the surface of the thin plate using ethyl cyanoacrylate adhesive (LOCTITE-401), which is curable at room temperature. The sensor was located on an axis across the center of the circular thin plate. Thus, the SMS sensor bend synchronously with the thin plate as air pressure is applied to the thin plate. Fiber optic jumpers used to connect optical devices and instruments are secured with tapes to minimize the small disturbance during the experiment. The loading of circular thin plate was realized by an air pressure loading device, which has a maximum pressure range of 250 kPa with an accuracy of 10 Pa. The circular thin plate structure was installed to the pressure inlet A of the device by screw thread. The inlet A was connected with a pressurized air chamber, the pressure of which can be adjusted roughly by hand pump. The rotating arm C2 can drive the alternate motion of piston to achieve the fine-tuning of the pressure of the pressurizing device. A pressure gauge with a digital display is installed on the inlet B for monitoring the input pressure, which is symmetrical to the pressure inlet A. The pressure can be removed directly to zero by turning the black knob (relief valve D) on the right.

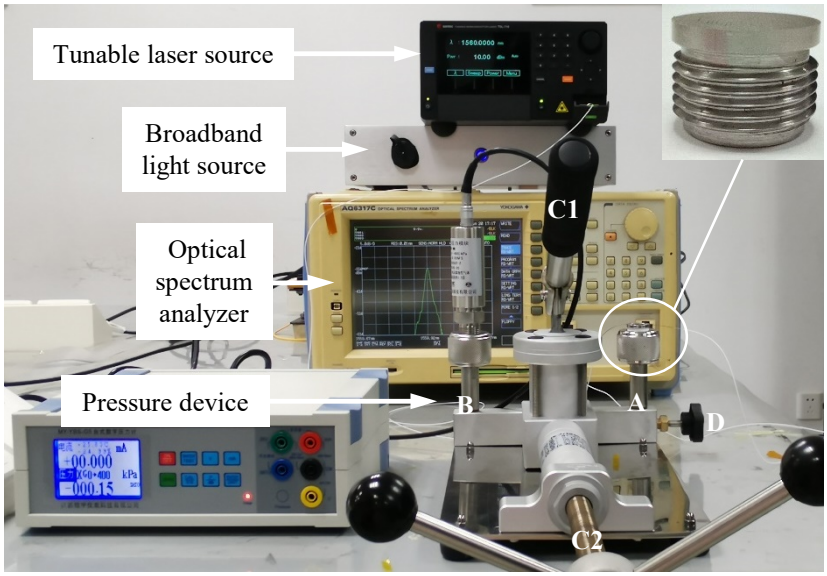

Fig. 12. The scheme of the air pressure measurement system. A: pressure inlet; B: pressure gauge; C1: hand pump; C2: rotating arm; D: relief valve.

In order to measure the variation of the transmission spectrum of the SMS sensor caused by air pressure, an ASE light source with a broadband wavelength range of 60 nm (1515 nm–1575 nm) and an optical spectrum analyzer (OSA, Yokogawa, AQ-6317C) were connected to the input and output ports of the sensor. The output spectra were recorded and investigated by the OSA. Moreover, the tunable laser (Santec, TSL-710) with a single wavelength output (rang: 1480 to 1640 nm) is used as a narrowband light source to analyse the sensing properties of the sensor. The TSL-710 has excellent wavelength characteristics with a narrow line width of 100 kHz, making it suitable for intensity-pressure detection. Compared with the measurement results of a broadband light source,

a pressure change can be converted to output power at a certain input wavelength by using a narrowband light source. In this way, low-cost intensity interrogation can be realized, which can be further applied to intensity measurement with a high sampling rate. One end of the SMS sensor is connected to this tunable laser, and the other end is connected to the OSA.

4.2. Analysis and discussion of experimental results

The SMS sensor was bonded on the circular thin plate, and the air pressure was controlled from 0 kPa to 130 kPa by the rotating arm. A step load of 10 kPa was applied and the transmission spectrum of the SMS sensor under each level loading was recorded. In order to reduce the effect of noise burr on the transmission spectrum, a local regression is performed using weighted linear least squares and a 2nd degree polynomial model to smooth the measured spectral data.

4.2.1. Results using broadband light source

Fig. 13 shows the measured transmission spectra of the SMS sensor at different air pressures. It can be seen that when the air pressure increases from 0 kPa to 130 kPa (as shown by the black arrow), the transmission spectrum has a significant blue shift and the intensity of spectral notch (Dip1) also decreases gradually. This evolution trend of monitored Dip1 is consistent with the simulated results which were displayed in Fig. 11 (b).

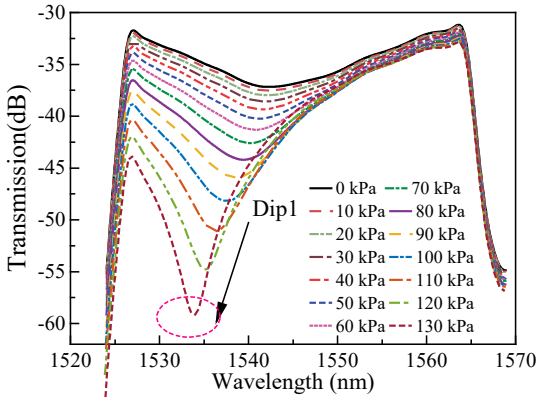

Fig. 13. Transmission spectral responses measured by the sensor as a functions of different air pressure.

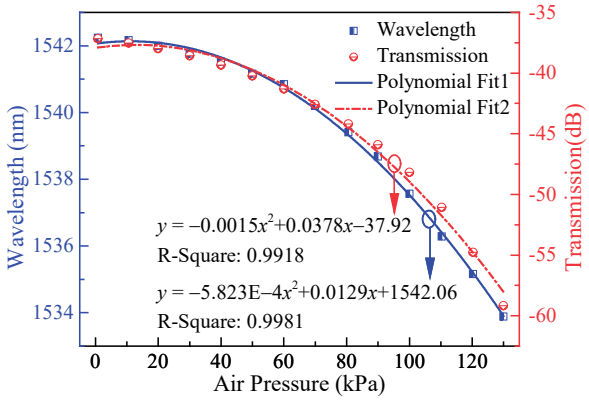

Fig. 14. Air pressure responses of Dip1 wavelength-pressure (blue line) and intensity-pressure (red line).

Both the wavelength shifts and transmission loss of the notch (Dip1) of the spectral response are demonstrated in Fig. 14. The wavelength shift of the Dip1 to the pressure response can be obtained by a polynomial fit, and the fitting curve exhibits a determination coefficient (R-square) of 0.9981. The total wavelength shifts were −8.36 nm in the air pressure range of 0–130 kPa, while the maximum pressure sensitivity (maximum absolute value of the derivative of the fitted curve) was calculated to be −138.5 pm/kPa. In addition, in the range of small pressure, about 0–60 kPa, the wavelength-pressure respond is quite linear, indicating that it can be characterized by a linear fit. Similarly, linear fitting can also be used in a larger pressure range of 70–130 kPa. The sensitivity for low air pressure is −24.2 pm/kPa, but has a high sensitivity, −106.7 pm/kPa in the large pressure, which were plotted in Fig. 15 (a). Compared to the sensitivity of the normal FBG of 4.67 pm/kPa, this result is significantly greater than that of FBG.

As shown in Fig. 14, the minimum intensity in the transmission spectrum is also negatively related to air pressure. The polynomial fitting results of the pressure sensing characteristics of the intensity of Dip1 in the spectrum were plotted, which exhibits the R-square of 0.9918. The fluctuation of the spectrum was around

−21.992 dB corresponding to 130 kPa, and the maximum pressure sensitivity (maximum absolute value of the derivative of the fitted curve) was −0.3522 dB/kPa. Moreover, the pressure sensitivity in a small pressure range (0–60 kPa) and a large pressure range (70–130 kPa) can be obtained to be −0.069 dB/kPa and −0.2718 dB/kPa by using the two linear fitting function, respectively, as shown in Fig. 15 (b).

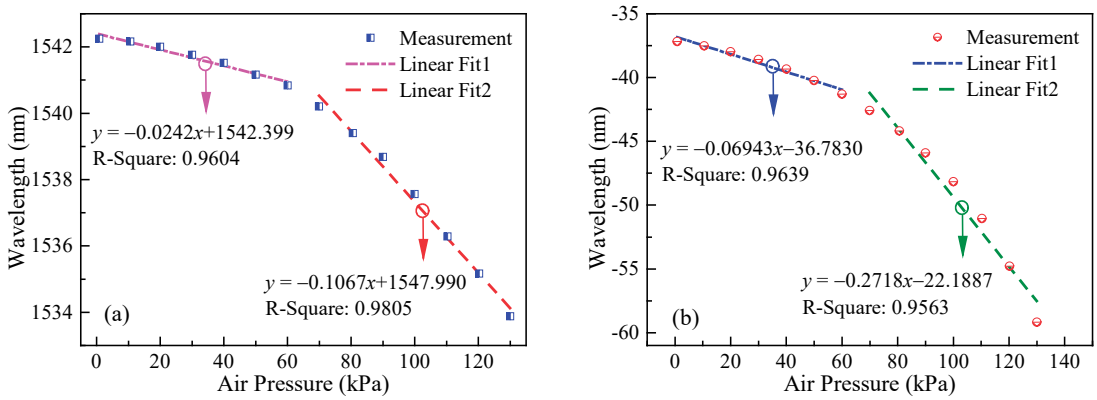

Fig. 15. Results of linear fitting. (a) Fitting curve result of the Dip1 wavelength shift against pressure variation; (b) Fitting curve result of the Dip1 intensity change against pressure variation.

Since the OSA used in the experiment has a wavelength resolution of 10 pm and a power measurement resolution of 0.001 dB. The minimum slopes of the response of the system are −24.2 pm/kPa and −0.069 dB/kPa, respectively, and hence the resolutions are 0.413 kPa and 0.0145 kPa in the small air pressure range from 0 to 60 kPa. While the resolutions are 0.0937 kPa and 0.0037 kPa in the large air pressure range from 70 to 130 kPa. It is worth noting that as the air pressure is greater than 130 kPa, the intensity of the notch (Dip1) of the transmission spectrum is less than −70 dB, which cannot be detected by the OSA, so the air pressure measurement range is 0–130kPa. To investigate the repeatability of the pressure measurement of the SMS sensor, the repeated experiments were performed three times with increasing pressure, as shown in Fig. 16. By analysing the wavelength shifts and light identity variations in the loading process, it can be concluded that the three measurement results are basically consistent without obvious changes. The measurement results indicate that the SMS sensor has good repeatability.

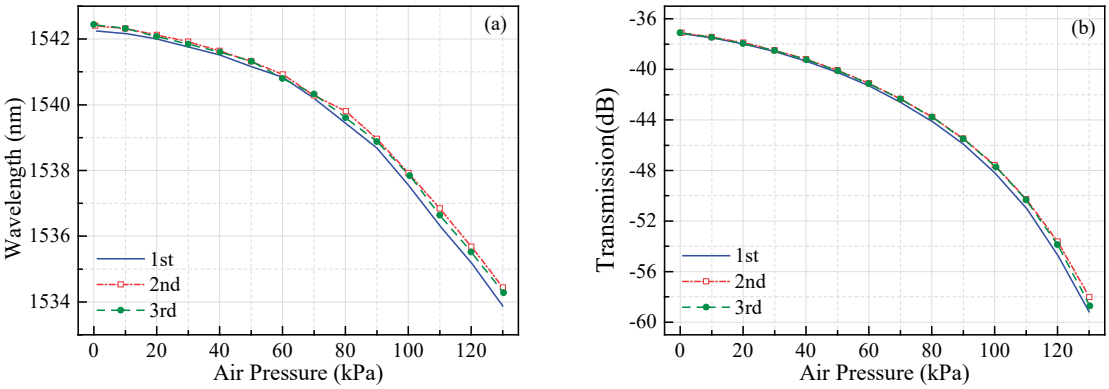

Fig. 16. Repeatability in three times tests of the (a) wavelength-pressure and (b) intensity-pressure.

The hysteresis characteristics of the sensor for pressure measurement are analyzed according to the different output values of the sensor under the same load in the loading and unloading process. The pressure was loaded to 130 kPa by the rotating arm with a 10 kPa step, and then unloaded with the same step. The transmission spectrum of the SMS sensor under each level of load was recorded. The wavelength and intensity change curves

corresponding to Dip1 of the measured spectrum are shown in Fig. 17. By observing a cycle of loading or unloading, no significant hysteresis in the measured wavelength shift and intensity variation were detected. The maximum hysteresis errors are 2.995% and 1.226% respectively, which occur at 84 kPa and 72 kPa loads respectively. These results indicate that the hysteresis of the sensor for air pressure measurement is very low. This result is reasonable, mainly due to the pressure measurement was carried out at room temperature, and there is no coating layer outside the SMS sensor. Within the pressure range in the experiment, the bending of the thin metal plate and the sensor are synchronized in the elastic stage. Thus, the hysteresis of the sensor for air pressure measurement is similar to that of a thin plate.

In order to investigate the effect of temperature against the SMS sensor, the wavelength shifts and the intensity changes of the spectra with respect to the temperature were also measured. The fabricated sensor was loosely sheathed in a polyimide sleeve to avoid strain and bending, and it can ensure that the temperature surrounding the SMS sensor uniformly increases. The sensor is in contact with a hot plate which temperature is controlled in the range of 25–75℃, with 3℃ steps. The temperature is monitored by a digital temperature meter while the output spectra of the sensor were recorded by the OSA. The wavelength shifts and intensity variations at different temperatures were characterized, as shown in Fig. 18. It can be seen from the measurement result (dot line), the wavelength shifts are approximately linear with temperature with positive slopes. The slope of the linear fitting curve is 7.02 pm/℃ in a temperature range of 25–75 °C. It should be noted that the intensity variation of Dip1 exhibits a significant change disorderly and the fluctuation is 0.0309 dB as the temperature is increased. When the temperature rises from 31 °C to 34 °C, the maximum intensity is 0.0148 dB. The ratio variation induced by temperature is ΔR_T (pm/℃ or dB/℃), then the measurement error caused by temperature can be expressed as $\Delta R_T/\Delta S$, where ΔS (pm/kPa or dB/kPa) is the slope of the respond to pressure. In the experiments, the maximum error due to temperature change is −0.29 kPa (7.02 /−24.2) and −0.0715 kPa (0.0148/3/−0.069). The temperature variation results in a change in pressure under test, therefore the temperature coefficient should be known, and the coefficient matrix equations for temperature-pressure can be used for spectral calibration to ensure the accuracy of the measurement.

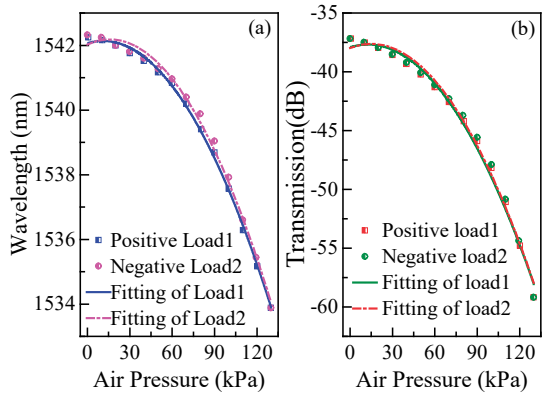

Fig. 17. Sensor hysteresis curve under loading and unloading of the (a) wavelength-pressure and (b) intensity-pressure.

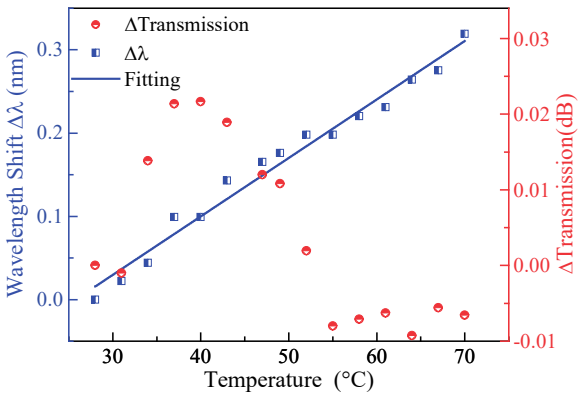

Fig. 18. Measured curve of the (a) wavelength shift-temperature and (b) intensity variation-temperature.

We can obtain the intensity changes of the transmission spectrum at different wavelengths of 1529 nm, 1531 nm, 1535 nm and 1538 nm from Fig. 13, and the results were illustrated in Fig. 19. At 1531 nm, the intensity changes monotonously and the sensitivity is higher than corresponding to 1529 nm. At 1535 nm, an inflection

point appears in the change of intensity under a pressure of 120 kPa. The intensity change corresponding to the center wavelength of 1538 nm is non-monotonically decreasing within the pressure measurement range. It can be concluded that the intensity variation of the sensor is dependent on the wavelength which is used to interrogate its respond. The slopes of the intensity-pressure curve are different at these several wavelengths. Therefore, according to this principle, the pressure measurement with different sensitivities can be achieved by fixing the output wavelength of the narrowband light source.

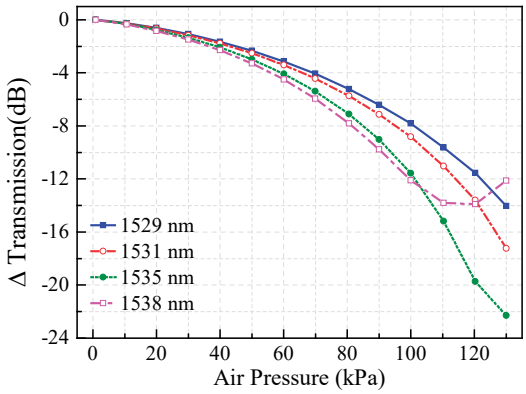

Fig. 19. The intensity variation of transmission spectrum with different wavelengths.

4.2.2. Results using narrowband light source

According to the analysis results in Fig. 19, a narrowband light source with a fixed output wavelength of 1531 nm was connected to the input end of the SMS sensor instead of the broadband light source. The output end is connected to the optical spectrum analyzer to measure the transmission spectrum under different air pressures, as shown in Fig. 20. With the increase of air pressure, the maximum intensity of the peak of the transmission spectrum decreases gradually. The polynomial fitting curve of the intensity-pressure of the peak in the spectrum is drawn in Fig. 21, with an R-squared of 0.9944. Moreover, the piecewise linear fitting is performed to calculate the pressure sensitivity in a small pressure range (0–60 kPa) and a large pressure range (70–130 kPa), they are −0.0531 dB/kPa and −0.1913 dB/kPa, respectively, as displayed in Fig. 21. The minimum slope of the system response is −0.0531 dB/kPa, combined with the resolution of the OSA used in the experiment, thus, the measurement resolution is 0.019 kPa and 0.0052 kPa in the small and large pressure ranges, respectively. It is estimated by polynomial fitting that when the pressure is greater than 210 kPa, the OSA cannot detect the intensity of the peak, so the air pressure measurement range is 0–210 kPa.

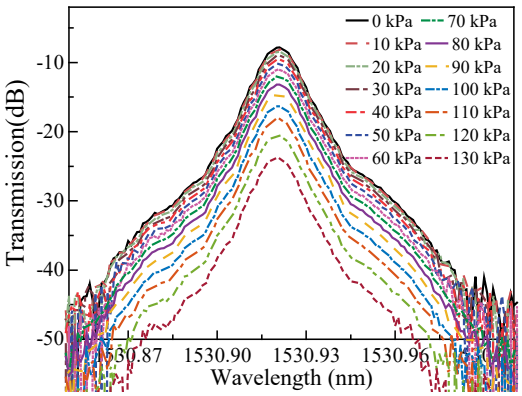

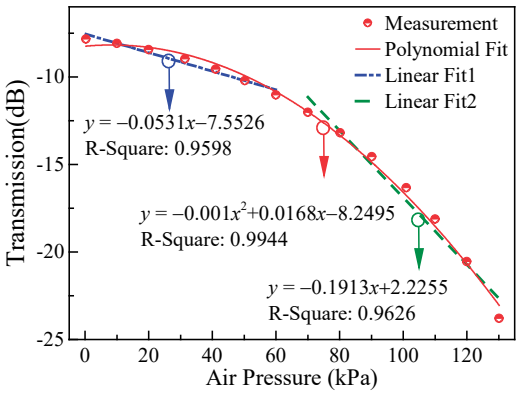

Fig. 20. Transmission spectral response measured by the sensor at 1531 nm.

Fig. 21. Repeatability in three times tests of the intensity-pressure.

Experiments were repeated three times to confirm the repeatability of the measurement pressure of the sensor under the narrowband light source. As shown in Fig. 22, the responses of each measurement were overlapped with each other, showing good repeatability. The maximum hysteresis errors are 1.213%, 1.404% and 0.625% observed under 130 kPa, 83 kPa and 40 kPa, respectively. By applying the linear fitting and monitoring the changes of the intensity for temperatures ranging from 25 ℃ to 75 ℃, the intensity of the peak was represented in Fig. 23. The slope of the intensity variation-temperature is 0.00237 dB/℃. The maximum measurement error caused by temperature was calculate to be −0.0446 kPa in a small pressure range (0–60 kPa) by using the previous definition. It should highlight that the intensity of peak does not exhibit a significant effect to the pressure measurement as the temperature is increased.

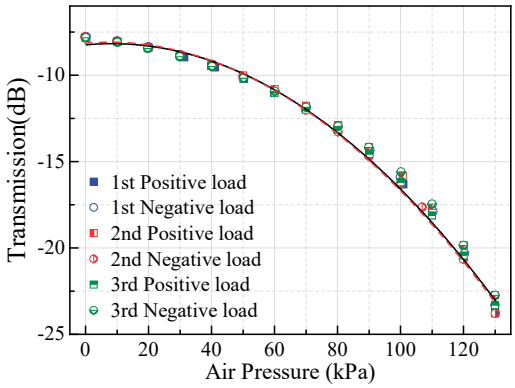

Fig. 22. Sensor hysteresis curve under loading and unloading of the intensity-pressure.

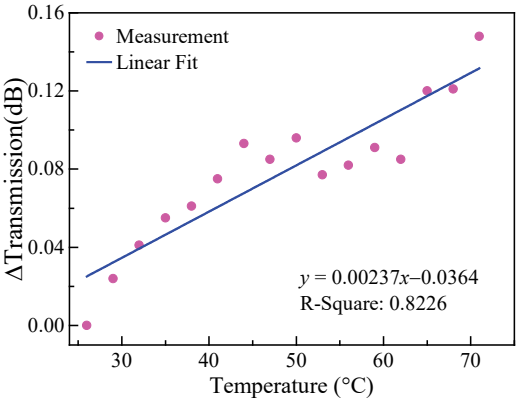

Fig. 23. Measured curve of the intensity variation-temperature.

In summary, the sensor based on multimode fiber can be used to measure the air pressure on the circular thin plate. By analyzing the test results, it can be seen that the sensor has relatively higher sensitivity, good repeatability and hysteresis. When the broadband light source is the input light field, both the central wavelength and intensity can be used to measure the air pressure at the same time, which provides guidance for further improving the high sensitivity measurement under small air pressure. The spectral response of the sensor analyzed in the above section can be measured by the optical spectrum analyzer. When the input light source is a narrowband light source, only the intensity change can be used as a signal for measuring air pressure. The light intensity can be converted into an electrical signal through the photodetector, which is connected to a collection card with a high sampling rate. This will be applied to the measurement of high-frequency dynamic signals.

5. Conclusions

This paper reports the measurement of the pressure of circular thin plate by an SMS optical fiber sensor, and the theoretical analysis and experimental verification are carried out. The bend applied to the MMF can effectively cause significant change of the output transmission power of the SMS fiber sensor. The sensor works on the basis of monitoring the wavelength and intensity changes of the SMS fiber sensor. The experimental results show that it is feasible to track the light intensity and wavelength of the transmission spectrum of the output end to measure the pressure changes of the thin plate structure with good sensitivity, repeatability and hysteresis. Within the

pressure range from 0 to 60 kPa, the intensity-pressure is −0.069 dB/kPa, and the wavelength-pressure is −24.2 pm/kPa, and it has a high sensitivity in large pressure range of 70–130 kPa at −0.2718 dB/kPa and −106.7 pm/kPa. The sensitivity is higher than that of the normal bare FBG, and it can be used for high sensitivity measurement at low air pressure. The intensity change of the transmission spectrum at a particular wavelength can also be used to measure pressure, with sensitivity of−0.0531 dB/kPa and −0.1913 dB/kPa, respectively, good repeatability and low hysteresis rate. This sensor can be applied to dynamic signal monitoring with high sampling rate requirement in structural health monitoring.

Acknowledgments

This research was supported by the Fund of Aeronautics Science (Grant Nos.: 20170252004, 20185644006, 20200009023017) and the Key Research and Development Plan of Jiangsu Province-Industrial Foresight and Common Key Technology (Competition Project) (Grant No.: BE2018047).

References

[1] E. Vorathin, Z.M. Hafizi, N. Ismail, M. Loman, Review of high sensitivity fibre-optic pressure sensors for low pressure sensing, Opt. Laser Technol. 121 (2020). doi:10.1016/j.optlastec.2019.105841.

[2] Y. Zhao, H. K. Zheng, R. Q. Lv, Y. Yang, A practical FBG pressure sensor based on diaphragm-cantilever, Sensors Actuators, A Phys. 279 (2018) 101–106. doi:10.1016/j.sna.2018.06.004.

[3] E. Vorathin, Z.M. Hafizi, A.M. Aizzuddin, M.K.A. Zaini, K.S. Lim, Temperature-independent chirped FBG pressure transducer with high sensitivity, Opt. Lasers Eng. 117 (2019) 49–56. doi:10.1016/j.optlaseng.2019.01.012.

[4] W.J. Bock, C. Jiahua, P. Mikulic, T. Eftimov, A novel fiber-optic tapered long-period Bragg grating sensor for pressure monitoring, IEEE Trans. Instrum. Meas. 56 (2006) 1176–1180.

[5] G.H. Chen, L.Y. Liu, H.Z. Jia, J.M. Yu, L. Xu, W.C. Wang, Simultaneous pressure and temperature measurement using Hi-Bi fiber Bragg gratings, Opt. Commun. 228 (2003) 99–105. doi:10.1016/j.optcom.2003.09.079.

[6] H.M. He, L. Wang, L.D. Yin, Asymmetric elliptical-hole dual-core photonic crystal fiber with enhanced pressure sensitivity, Opt. Fiber Technol. 20 (2014) 380–383. doi:10.1016/j.yofte.2014.04.009.

[7] C. Zhu, Y. Chen, Y. Zhuang, G. Fang, X. Liu, J. Huang, Optical interferometric pressure sensor based on a buckled beam with low-temperature cross-sensitivity, IEEE Trans. Instrum. Meas. 67 (2018) 950–955. doi:10.1109/TIM.2018.2791258.

[8] Y. Du, Y. Chen, C. Zhu, Y. Zhuang, J. Huang, An embeddable optical strain gauge based on a buckled beam, Rev. Sci. Instrum. 88 (2017). doi:10.1063/1.5004109.

[9] W.Y. Ma, Y. Jiang, J. Hu, L. Jiang, T.J. Zhang, Microelectromechanical system-based, high-finesse, optical fiber Fabry-Perot interferometric pressure sensors, Sensors Actuators, A Phys. 302 (2020) 111795. doi:10.1016/j.sna.2019.111795.

[10] Z. Zhang, J. He, B. Du, F. Zhang, K.K. Guo, Y. Wang, Measurement of high pressure and high temperature using a dual-cavity Fabry-Perot interferometer created in cascade hollow-core fibers, Opt. Lett. 43 (2018) 6009. doi:10.1364/ol.43.006009.

[11] Q. Wu, Y. Qu, J. Liu, J. Yuan, S. P. Wan, T. Wu, X. D. He, B. Liu, D. Liu, Y. Ma, Y. Semenova, P. Wang, X. Xin, G. Farrell, Singlemode-multimode-singlemode fiber structures for sensing applications–A review, IEEE Sens. J. XX (2020). doi:10.1109/JSEN.2020.3039912.

[12] Q. Wu, Y. Semenova, P. Wang, G. Farrell, Fiber heterostructure for simultaneous strain and temperature measurement, Electron. Lett. 47 (2011) 713–714. doi:10.1049/el.2011.0974.

[13] Q. Wu, Y. Semenova, P. Wang, G. Farrell, High sensitivity SMS fiber structure based refractometer–analysis and experiment, Opt. Express. 19 (2011) 7937. doi:10.1364/oe.19.007937.

[14] E. Li, Sensitivity-enhanced fiber-optic strain sensor based on interference of higher order modes in circular fibers, IEEE Photonics Technol. Lett. 19 (2007) 1266–1268. doi:10.1109/LPT.2007.902271.

[15] Y. Gong, T. Zhao, Y.J. Rao, Y. Wu, All-fiber curvature sensor based on multimode interference, IEEE Photonics Technol. Lett. 23 (2011) 679–681. doi:10.1109/LPT.2011.2123086.

[16] J. Huang, X.W. Lan, H.Z. Wang, L. Yuan, T. Wei, Z. Gao, H. Xiao, Polymer optical fiber for large strain measurement based on multimode interference, Opt. Lett. 37 (2012) 4308. doi:10.1364/ol.37.004308.

[17] Y.H. Qi, L. Ma, Z.X. Kang, Y.L. Bai, B. Yin, S.S. Jian, Highly sensitive curvature sensor based on a multicladding fiber sandwiched dual no-core fibers structure, Appl. Opt. 53 (2014) 6382. doi:10.1364/ao.53.006382.

[18] L. Ma, Y.H. Qi, Z.X. Kang, S.S Jian, All-fiber strain and curvature sensor based on no-core fiber, IEEE Sens. J. 14 (2014) 1514–1517. doi:10.1109/JSEN.2014.2298553.

[19] Y. Zhao, L. Cai, X.G. Li, Temperature-insensitive optical fiber curvature sensor based on SMF-MMF-TCSMF-MMF-SMF structure, IEEE Trans. Instrum. Meas. 66 (2017) 141–147. doi:10.1109/TIM.2016.2615479.

[20] Q. Wang, Y. Liu, Optical fiber curvature sensor based on MMF-SCF-MMF structure, Opt. Fiber Technol. 43 (2018) 1–5. doi:10.1016/j.yofte.2018.03.010.

[21] D.A. May-Arrioja, V.I. Ruiz-Perez, Y. Bustos-Terrones, M.A. Basurto-Pensado, Fiber optic pressure sensor using a conformal polymer on multimode interference device, IEEE Sens. J. 16 (2016) 1956–1961. doi:10.1109/JSEN.2015.2510360.

[22] Y.N. Pang, B. Liu, J. Liu, S.P. Wan, T. Wu, X.D. He, J. Yuan, X. Zhou, K. Long, Q. Wu, Wearable optical fiber sensor based on a bend singlemode-multimode-singlemode fiber structure for respiration monitoring, IEEE Sens. J. 21 (2020) 4610–4617. doi:10.1109/JSEN.2020.3032646.

[23] Q. Wu, M. Yang, J. Yuan, H.P. Chan, Y. Ma, Y. Semenova, P. Wang, C. Yu, G. Farrell, The use of a bend singlemode-multimode-singlemode (SMS) fibre structure for vibration sensing, Opt. Laser Technol. 63 (2014) 29–33. doi:10.1016/j.optlastec.2014.03.015.

[24] L.B. Soldano, E.C.M. Pennings, Optical multi-mode interference devices based on self-imaging: principles and applications, J. Light. Technol. 13 (1995) 615–627. doi:10.1109/50.372474.

[25] W.S. Mohammed, A. Mehta, E.G. Johnson, Wavelength tunable fiber lens based on multimode interference, J. Light. Technol. 22 (2004) 469–477. doi:10.1109/JLT.2004.824379.

[26] M. Heiblum, J.H. Harris, Analysis of curved optical waveguides by conformal transformation, IEEE J. Quantum Electron. 11 (1975) 75–83. doi:10.1109/JQE.1975.1068563.

[27] A. Iadicicco, D. Paladino, M. Moccia, G. Quero, S. Campopiano, W.J. Bock, A. Cusano, Mode coupling and field distribution in sub-mm permanently bent single mode optical fibers, Opt. Laser Technol. 47 (2013) 292–304. doi:10.1016/j.optlastec.2012.08.012.

[28] C. Sun, M. Wang, J. Liu, S. Ye, L. Liang, S. Jian, Fiber ring cavity laser based on modal interference for curvature sensing, IEEE Photonics Technol. Lett. 28 (2016) 923–926. doi:10.1109/LPT.2016.2517666.

[29] E. Ventsel, T. Krauthammer, Thin Plates and Shells: Theory, Analysis and Application, Marcel Dekker Inc., New York, 2001.

[30] P. Kelly, Solid mechanics part I: an introduction to solid mechanics, Solid Mechanics Lecture Notes, University of Auckland.

[31] Q. Wang, G. Farrell, Numerical investigation of multimode interference in a multimode fiber and its applications in optical sensing, Opt. Sens. II. 6189 (2006) 61891N. doi:10.1117/12.662197.

[32] P.A. Besse, M. Bachmann, H. Melchior, L.B. Soldano, M.K. Smit, Optical bandwidth and fabrication tolerances of multimode interference couplers, J. Light. Technol. 12 (1994) 1004–1009. doi:10.1109/50.296191

[33] X. Wang, E. Lewis, P. Wang, Investigation of the self-imaging position of a singlemode-multimode-singlemode optical fiber structure, Microw. Opt. Technol. Lett. 59 (2017) 1645–1651. doi:10.1002/mop.30605.

[34] P. Wang, S. Zhang, R. Wang, G. Farrell, M. Zhang, T. Geng, E. Lewis, K. Tian, Temperature-insensitive refractometer based on an RI-modulated singlemode-multimode-singlemode fibre structure, Opt. Express. 27 (2019) 13754. doi:10.1364/oe.27.013754.

[35] T. Geng, S. Zhang, F. Peng, W. Yang, C. Sun, X. Chen, Y. Zhou, Q. Hu, L. Yuan, A temperature-insensitive refractive index sensor based on no-core fiber embedded long period grating, J. Light. Technol. 35 (2017) 5391–5396. doi:10.1109/JLT.2017.2772304.